Computational Fluid Dynamics Study of the Effect of Leg Position on Cyclist Aerodynamic Drag

Martin D. Griffith, Timothy Crouch, Mark C. Thompson, David Burton, John Sheridan

Fluids Laboratory for Aeronautical and Industrial Research (FLAIR)

Department of Mechanical and Aerospace Engineering

Monash University

Melbourne, Australia 3800

Email: martin.d.griffith@gmail.com

Nicholas A. T. Brown

Australian Institute of Sport

Belconnen, Canberra, Australia, 2617

ABSTRACT

An experimental and numerical analysis of cycling aerodynamics is presented. The cyclist is modelled experimentally by a mannequin at static crank angle; numerically, the cyclist is modelled using a CAD reproduction of the geometry. Wind tunnel observation of the flow reveals a large variation of drag force and associated downstream flow structure with crank angle; at a crank angle of 15°*, where the two thighs of the rider are aligned, a minimum in drag is observed. At a crank angle of* 75°*, where one leg is at full extension and the other is raised close to the torso, a maximum in drag is observed. Simulation of the flow using computational fluid dynamics (CFD) reproduces the observed variation of drag with crank angle, but under-predicts the experimental drag measurements by approximately* 15%*, probably at least partially due to*

simplification of the geometry of the cyclist and bicycle. Inspection of the wake flow for the two sets of results reveals a good match in the downstream flow structure. Numerical simulation also reveals the transient nature of the entire flow field in greater detail. In particular it shows how the flow separates from the body of the cyclist which can be related to changes in the overall drag.

1 INTRODUCTION

When cycling at high speed on a flat gradient, such as in racing, aerodynamic drag can account for up to 90% of the resistance experienced by the cyclist [1, 2]. The drag force, D, is defined by:

$$D = 0.5\rho U^2 C_D A, \tag{1}$$

where ρ is the density of air, U is the cyclist velocity relative to the fluid, C_D is the coefficient of drag and A is the frontal area of the cyclist. At high speed, the cyclist can reduce the drag experienced by minimizing frontal area, A, or by configuring their position to achieve a flow minimizing drag coefficient, C_D. Any approach taken must be balanced with the optimal rider position for power output, as well as being within the rules set by the competition regulators.

Wind tunnel testing of cycling aerodynamics is often used to test the aerodynamic performance of elite cyclists. Computational fluid dynamics (CFD) is an additional tool for detailed analysis of flow and aerodynamics. An advantage of CFD is its capacity to provide highly resolved velocity and pressure distributions over the entire space surrounding the cyclist, which allows a more detailed analysis of the factors affecting performance. There is only limited work on cyclist aerodynamics using CFD in the literature [3–7]; from a fluid dynamics perspective, the problem is a complex one. The rider-bicycle geometry is three-dimensional, consisting of a large variety of surfaces, arrayed at a variety of angles to the oncoming flow and across a wide range of length scales. There are no exploitable geometric symmetries to simplify the computational model. Furthermore, the geometry position and shape vary with the pedaling action. The main limiting factor for a CFD model of a turbulent three-dimensional flow is the computational hardware needed to solve the flow with adequate accuracy. Resolving every length

scale of the problem in the model requires a large amount of computational resources. Simplifications to the geometry and modelling of turbulence associated with smaller length scales are necessary. The selection of an appropriate turbulence model for the application is essential. The accuracy of the model needs to be assessed, usually by comparison with experimental results. Significant overheads are also associated with mesh generation.

Reference [4] presents an analysis of the flow past a rider at fixed leg position without a bicycle using CFD, employing both steady-state RANS (Reynolds-Averaged Navier-Stokes) with the standard $k-\varepsilon$ turbulence model, and transient simulations with the LES (Large Eddy Simulation) turbulence modelling approach. Simplifying the problem by using a fixed leg position renders the CFD modelling significantly more tractable, due chiefly to the difficult challenges in incorporating mesh movement and deformation. Fair agreement was found between CFD and wind tunnel experiments [4]; however, without the inclusion of a bicycle in the computational model, the drag comparison between the two sets of results relied on the drag force on the bicycle alone being comparable to the contribution to total drag of the bicycle within the coupled bicycle and cyclist geometry. This assumption may be approximately valid, but is difficult to test. Surface pressure was also compared favourably between the two sets of results; however, no comparison of the wake flow structure was made.

In a later paper, [5] simulated a scaled-down cyclist model, substituting the bicycle for an aerofoil-shaped stand. They tested a variety of turbulence-modelling approaches, concluding that of the RANS approaches, the Shear-Stress Transport (SST) $k-\omega$ approach achieved the best overall performance in terms of matching drag, lift and pitch areas obtained from wind-tunnel tests. This emperical determination of the most suitable turbulence modelling approach agrees with experience of the SST model at large; for bluff body flows, characterised by large wakes and indeterminate flow separation, the SST model appears to be becoming the preferred method [8]. Further work in [6] has examined the drag and heat transfer characteristics of specific components of the rider geometry.

Analyzing the static, fixed leg cases provides a useful starting point to establishing the fundamental flow characteristics, and the current study uses the same approach. An important issue is the relevance of the flow for the static leg case to that of the pedaling case; will the flow measured for a rider in static position share similar features with the flow obtained with a moving leg model, at the appropriate phase of the crank angle cycle? Given the low velocity of the legs (for a standard pedalling cadence

of approximately 1.4Hz) compared to the oncoming flow, it is not unreasonable to assume that a quasi-steady assumption holds. This is a question not directly addressed in the literature. An ultimate goal of the current work is to develop a dynamic, pedalling cyclist CFD model. However, a first step – both in addressing the research question and in progressively developing our computational model – is to obtain an understanding of the variation of the flow with (static) crank angle. Varying the crank angle leads to significant changes in the shape and position of the legs. Understanding the effect and extent of these variations on the flow will be useful in evaluating the quasi-steady assumption, but also in assessing the importance of other changes or simplifications to the geometry that numerical modeling entails.

The current paper has three aims: (i) to build upon earlier wind-tunnel based work in our group [9] and further characterize the variation of the flow with crank angle, (ii) to compare flow behaviour observed experimentally with CFD results, in order to assess the current capability to numerically model cyclist aerodynamics, and (iii) to build a foundation from which the more challenging problem of a dynamic, pedalling cyclist CFD model can be developed.

2 METHOD

All flows were run with a freestream velocity $U = 16$ m/s, or 57.6 km/h and with a cyclist in a static riding position. Figures 1 and 2 show the experimental and numerical models tested. Crank angles were measured with the reference crank angle, $\theta = 0^\circ$, located where the left foot is at its farthest position downstream, or, where the pedals are level and the right foot is towards the front of the bicycle. In the streamwise or x-direction, $x = 0$ is defined as co-located with the rear axle of the bicycle.

2.1 Experiments

Using wind tunnel observation, characterisation of the variation of the flow with static crank angle has been reported in [9] and [10]. The approach taken was to manufacture a posable mannequin based on a generic cyclist. The option of using an actual cyclist rather than a mannequin was considered, but initial testing revealed difficulties with repeatability of results. Consistent cyclist positions over the crank cycle, both throughout testing and from one test to the next, could not be maintained. Selecting a mannequin as the cyclist overcame these problems. The mannequin shape was determined in collaboration with the Australian Institute of Sport, and is based on their best estimates of the body size and

shape of elite track cyclists. The mannequin was built to provide rotation at the hips and knees, allowing the full range of crank positions to be tested. The ankle was fixed with the foot aligned perpendicular to the shank. A standard track bicycle was used.

The mannequin was placed in the 1.4 megawatt Monash Large Wind Tunnel at Monash University. The turbulence intensity in the middle of the 3/4 open jet test section of the wind tunnel is 1.6% and the blockage ratio based on the frontal area of the mannequin and bicycle and the jet exit area of the is $< 4.0\%$. Measurements of the time-averaged three component velocity field were taken using a four hole dynamic pressure probe (TFI Cobra probe), with the position of the probe controlled with a two axis traverse. Measurements were taken on and behind the body of the cyclist in planes perpendicular to the direction of flow, with each measurement sampled at 1250Hz for 15 seconds. A six component Kistler force balance of the piezoelectric type enabled the measurement of drag and lift forces experienced by the model. Force measurements were taken as the mean of three separate tests sampled at 500 Hz for 30 seconds. Assuming a normally distributed error, the uncertainty in the experimental drag area measurements is $\pm 0.003 \mathrm{m}^2$.

2.2 Numerical Simulations

The numerical model of the rider is created from the same specifications as the experimental mannequin from [10], excepting the head and helmet, which were taken from a scan. Scanning the entire experimental model for use in the simulations was a possibility, but was rejected. There are two main advantages in defining the torso, arm and leg geometries using CAD (computer-aided design) software. Firstly, having a well-defined and controlled CAD model allows the geometry to be easily adjusted to test the effect of variation of, for example, forearm position, torso angle or leg position/crank angle. Secondly, the ultimate goal in building the computational model is to achieve a geometrically dynamic CFD simulation with a pedalling cyclist. Essentially, our CFD model must be capable of producing any geometry over the 360° range of the crank angle cycle. This will require precise solid body rotation and translation of the thighs and shanks, which are more readily defined and moved within a CAD model than in a 3D scan. Some details of the experimental model were not reproduced exactly, with the more muscled mannequin arms being depicted with simpler tapered cylindrical and elliptical sections. For reasons of protection of intellectual property, the bicycle used experimentally was not recreated

numerically; rather, a generic bicycle model was generated, with the sections and major dimensions representative of a standard track bicycle. An approximation of the wide handlebars seen on the experimental model was included on the numerical model. The struts on the front axle were not included; the more substantial support on the rear axle was included. The wheels were modelled without spokes. The effect of spokes on the drag force experienced by an isolated bicycle wheel was investigated by [11]. They found that increasing the number of spokes in the wheel from 8 spokes to 32 spokes could increase the force experienced by the wheel by up to 25%. The effect may be less certain however, in considering the wheel as a component of an entire cyclist and bicycle geometry.

Flows were simulated with the commercial CFD software, ANSYS–CFX, which employs a conservative finite-volume based control volume method to solve for the Navier-Stokes equations for fluid flow. The numerical results presented in this paper were obtained using both RANS and transient simulations. Of the RANS solvers, the Shear Stress Transport (SST) $k-\omega$ turbulence model is best suited for strongly three-dimensional separated flow [8], such as seen in the flow over a cyclist. The SST turbulence model was developed specifically for application to fluid flow problems characterised by strong adverse pressure gradient and separation. For similar reasons, for transient solutions, the Scale-Adaptive Simulation Shear Stress Transport (SAS-SST) model [12] was judged to be the most suitable of the available turbulence models for transient simulations. In near-wall regions, the model reduces to the same treatment and mesh requirements as the RANS SST model, while in unsteady regions of the flow (such as in separated flow in the cyclist wake) a "LES-like" behaviour results. The similarity in method between SST and SAS-SST is useful in allowing the same meshes to be used for both RANS and transient simulations, with the RANS solution also providing a suitable starting solution for the transient run. Other hybrid turbulence modeling methods for transient simulations using LES approaches are available and feasible for the current problem [13, 14]; however, the decision to use SAS-SST was based on the methods available and also the ability to be easily integrated into an ongoing study already employing RANS SST. Had there been a wider scope to the project such alternative methods could have been investigated. As is recommended for separated flows, boundary layers were resolved down to the wall; y^+ values were less than 1 over the cyclist model. This constraint is suitable for both the SST and SAS-SST simulations.

Domain boundaries were placed far enough from the cyclist that their position had a negligible

effect on the results. The road, represented by the lower domain boundary, was modelled as a wall with a velocity matching the freestream velocity, U. The inlet was placed 10m upstream of the rider, while the remaining streamwise boundaries were also set 10m from the rider. This resulted in a blockage ratio of approximately 0.2%. The outlet length was set at 40m. Solutions with even larger clearances between the rider and the domain boundaries produced negligible differences in the flow near the cyclist.

The meshes used to produce the results of this paper consist of approximately 33 million elements. The highly three-dimensional cyclist geometry meant that an unstructured mixed mesh was used, featuring prismatic elements within the boundary layers of the cyclist and bicycle, transitioning to tetrahedral elements away from the boundary layer and finally to regular hexahedral elements in the far field. Over the cyclist-bicycle geometry, 35-40 element layers were included in the fluid boundary layer, which typically required an inflation rate of 1.05. A grid resolution study was undertaken on the steady-state simulations, whereby resolution of the surface elements on the rider surface was increased, up to a maximum size of 55 million elements. No change greater than 2% in measured mean lift or drag forces was found at the higher resolutions tested than that used for the results presented here, for both steady and transient simulations. All solutions were iterated until the root-mean-squared residual quantities were of the order of 10^{-5}. For transient simulations, adaptive timestepping was used to obtain a timestep of 4×10^{-4} seconds, with 5 iterative loops per timestep; timestep sensitivity was then tested down to a timestep of 1×10^{-4} and no appreciable difference was observed in the mean behaviour of the force measurements or vorticity fields.

Each simulation was run in parallel on 64 nodes, using high-performance computing hardware at the National Computational Infrastructure (NCI) National Facility in Canberra, Australia. Each steady-state run took up to 300 hours in total computing time, while transient simulations would take approximately 6000 hours per second of simulation time.

3 RESULTS AND DISCUSSION

In order to assess the validity of the numerical modelling used, figure 3 plots the variation of drag with crank angle, θ, for both the experiments and the steady-state numerical simulations. The quantity plotted is the *drag area*, $C_D A = \frac{D}{\frac{1}{2}\rho U^2}$, (where D is the drag force and ρ is the density of the fluid) which is often used as it does not require an explicit determination of the frontal area, A. Also, the drag area

is directly proportional to the drag force as the cyclist varies position. When considering drag area, it is important to note the contribution of both the frontal area and the flow, represented by the drag coefficient, C_D.

The numerical results under-predict the drag area measured in the wind tunnel throughout the crank cycle by between 13 and 17%. There are several possible explanations for this: the geometry used in the numerical model does not match exactly the model used experimentally; there are numerous small differences, such as the presence of spokes and additional struts to hold the experimental model in place. The surface roughness of the mannequin has not been included in the geometry for the numerical simulation. The bicycle of the numerical model is of a simpler design than that used experimentally; there has not been an exact replication of the handle bars in the numerical model. In addition, there may be some inaccuracy associated with the turbulence modeling, including fully resolving the flow and capturing the full separation. All of these factors have small effects, which cumulatively may cause a measurable departure from the measured drag.

However, where the numerical and experimental results strongly agree is on the variation of drag area with crank angle, with the error consisting of an offset to the whole data set. Minima in drag are observed at crank angles of $\theta \approx 15^\circ$ (and the equal but opposite geometry of $\theta \approx 195^\circ$). These crank angles correspond to rider positions where the thighs of the rider are even with each other (see the numerical model sketched in figure 2). Both sets of results show a maximum in drag around a crank angle of $\theta = 75^\circ$ (and the equal but opposite geometry of $\theta = 255^\circ$). These are the crank angle positions where one leg is almost straight and the other is tucked up, with the thigh close to the torso. Since figure 3 presents values of drag area, C_DA, the variation can be attributed to both changes in the flow (C_D) and the change in frontal area of the geometry (A). Though not shown here, the frontal area of the geometry over the crank angle range has been calculated, and though the frontal area varies through the cycle, its variation accounts for no more than 5% of the variation in C_DA seen in figure 3, indicating a significant change in drag coefficient due to changes in the wake flow with crank angle.

To further assess the numerical model, figure 4 presents the wake flow, comparing the velocity probe data sweeps from the wind tunnel model, with the numerical results. Contours of streamwise vorticity, $\omega_x = \frac{\partial w}{\partial y} - \frac{\partial v}{\partial z}$, are plotted, giving an indication of the streamwise flow structure generated by the cyclist geometry. These swirling flow structures lead to increased drag on the cyclist - just as wingtip trailing

vortices do for aircraft. The vorticity is plotted in planes taken at three locations: 0.04m upstream of the rear axle and 0.32m and 0.60m downstream of the rear axle. The leftmost of each set of three images shows the experimental results, representing the time-averaged field. The middle of each set of three images shows contour plots obtained using the steady solver method (steady-state SST) used for the numerical results of figure 3. A visual comparison between the experimental results and the steady-state SST results for the high drag case of $\theta = 75^\circ$ is fair, with a bias of the wake flow to one side observed in both results. This geometry consists of two thighs in opposite configuration, which produces something approaching a cavity on one side of the geometry. The comparison for the low drag case of $\theta = 15^\circ$ is less good, with the upper-body symmetry of the time-averaged experimental flow not observed in the numerical solution.

Simulations were also undertaken using the SAS-SST turbulence model for transient simulations. These simulations are an order of magnitude more expensive computationally than the RANS simulations, and have been limited to simulating the low and high drag 15° and 75° crank angle cases. The values of drag area returned by the SAS-SST transient solver are not significantly different to those returned by the steady-state SST solver. However, the time-averaged wake flows compare better; figure 4 includes vorticity plots for solutions obtained with the transient SAS-SST solver. The results are time averages of a flow resolved in time, which more closely matches the methodology used experimentally. The simulations were run for approximately 5000 timesteps before time-averaging of the velocity field was begun, to allow the flow to fully develop; monitors of velocity and pressure in the flow were found to settle to quasi-steady state approximately 1000 timesteps after the simulation startup. The averaged velocity field converged after approximately 3000 timesteps, with further averaging producing negligible further changes in the time-averaged vorticity fields. For the 15° case, the time-averaged field for the transient simulation gives a better comparison with the wind tunnel measurements. Similar vorticity patterns are observed in the $x = 0.32$ m plane. At $x = 0.60$, the fields are still similar, only the numerical simulation seemingly has not matched the diffusion of the streamwise vortices further downstream. For the high drag $\theta = 75^\circ$ case, the comparison is slightly better than for the SST simulation.

To further explore the effect of time-averaging, figure 5 compares, for both the low and high drag cases, at left, the time-averaged streamwise velocity field with, at middle, a snapshot of the transient field at an arbitrary time. Also included, at right, are snapshots of the streamwise vorticity to compare with

the time-averages of figure 4. For the $\theta = 15^\circ$ case, the instantaneous velocity and vorticity fields do not closely resemble the time-averaged equivalents. For the $\theta = 75^\circ$ case, the instantaneous fields exhibit more well-defined structures than in the 15° case. The same left to right bias of the flow is evident, as well as the positive-negative vortex pair, seen in the time-averaged experimental and numerical fields from figure 4.

Given the significant difference in drag area seen between the 15° and 75° crank angle geometries, a difference between each case should be observable in the velocity defect downstream. The high drag case should exhibit in general lower streamwise velocities in the wake. This can be seen qualitatively in figure 5; the high drag case presents a stronger velocity defect than the low drag one. The defect appears to be centered on the main negative-positive vorticity concentrations evident in the corresponding instantaneous and time-averaged vorticity plots of figures 4 and 5. Further evidence of the defect can be seen in figure 6, which plots contours of time-averaged streamwise velocity in the $x-y$ plane for the low and high drag cases. Downward velocity vectors can be seen immediately downstream of the torso in the high drag $\theta = 75^\circ$ case, suggesting strong recirculation in this region behind and below the torso. It is worth noting again that the $\theta = 75^\circ$ case includes a thigh aligned almost perpendicularly with the flow direction, just behind the plane shown in figure 6. This appears to create a strong separation, in comparison with the corresponding thigh in the low drag $\theta = 15^\circ$ case, which is aligned closer to 45° with the flow. This evidently leads to less flow separation, which results in a reduced drag area.

These qualitative assertions are borne out in figure 7, which presents a breakdown of the individual contributions to total C_DA (plotted in figure 3) from components of the geometry. The ease with which this type of analysis can be obtained represents one of the key advantages of CFD. The drag area of the head and arms does not vary significantly over the crank cycle. The positions of these components do not vary and they are located upstream from the components that do; therefore little variation is expected. The legs are the only parts which vary in shape and orientation through the crank cycle and the drag area of each varies significantly. The peak drag area of either leg occurs at crank angles of $\theta = 75^\circ$ and 255°. At these crank angles, one leg is in an extended, almost straight position, while the other is flexed closer to the torso. On figure 3, in addition to the drag area, the variation of the angle of each thigh to the horizontal is also plotted. A higher thigh angle indicates a straightened leg, while a lower one indicates a tucked up one. The maxima in total drag area and drag area of an individual leg

correspond closely with the maximum extension of either of the legs. There is a significant difference in frontal surface area of each leg over the crank cycle, which may account for the variation seen for the legs in figure 7. However, the drag area of the torso also varies strongly over the crank cycle, with no change in frontal surface area.

For the high drag cases ($\theta = 75^\circ$ and 255°), one leg is almost straight and perpendicular to the flow. The position of the legs in the high drag case creates a surface at the rear of the geometry which is aligned perpendicularly to the oncoming flow, comprising of the leg and backside. It is reasonable to expect that such a bluff configuration will be less aerodynamically efficient and hence result in higher drag. The straightening of the leg interacts with the flow to increase the drag area on both the leg and the torso. In contrast, the low drag $\theta = 15^\circ$ case consists of two thighs aligned closer to 45° with the flow, which produces a rear surface more conducive to maintaining attached wake flow, and hence lower drag.

In order to better depict the topology of the wake flow of the high and low drag cases, figure 8 plots, for an instantaneous snapshot of the transient flow, an isosurface of the invariant q-criterion [15, 16], which is useful for elucidating three-dimensional vortical structures. At top, the symmetry in the wake flow observed earlier for the low drag case is evident. For the high drag case, the stronger separation off the straight right leg can be observed, with a strong swirling from the back of the right thigh reaching downstream.

These plots show a complex flow and it is difficult to pick flow structures from them with confidence. Figure 9 plots the same isosurface, but on the time-averaged field. Noise and turbulence are averaged out, and the stronger and persistent flow structures are evident; this gives a good picture of the aerodynamics of the high and low drag cases. For the high drag case, a strong positive vortex can be seen beginning at the back of the straight right thigh, with a paired negative vortex coming from the left thigh and in between the legs. What looks to be the corresponding vortex pair in the low drag case appears to detach from the backside and be of lesser strength. This indicates an attached flow up the back of the thigh; the torso and thighs are aligned in such a way that they form a wedge pointing downstream, leading to a better aerodynamic performance compared to the 75° case.

4 CONCLUSIONS

This paper has presented numerical and experimental data on the flow past a model of a cyclist, over a range of static leg positions. In all data sets, a dependence of drag on crank angle is observed, with high drag measurements corresponding to rider geometries with one leg extended to nearly full length and the other folded up close to the torso. The low drag cases corresponds to the rider position where both thighs are at the same angle. Focussing on what were identified as the low and high drag cases ($\theta = 15^\circ$ and 75°), numerically, transient simulations are found to provide good flow field comparisons with the experimental results. A shifting of the wake flow to one side for the high drag cases was observed, while for the low drag case, a more weakly defined wake structure was observed, the average of which gives a more symmetric flow field. The drag experienced by the rider seems to depend on the surfaces at the rear, with the alignment of either thigh perpendicular to the flow increasing the strength of the downstream vortical flow structures. The strength of the vorticity structure can be linked to the drag experienced by the cyclist. Using the CFD simulations, by examining the drag force on individual components, it was found that the positioning of the legs affected not only the drag force experienced by the legs, but also the drag force experienced by the rider torso, indicating a need for caution in considering components in isolation from the entire geometry.

Acknowledgements

This work was supported by the Australian Research Council, through the Linkage Project scheme (project number: LP100200090) and through the Australian Institute of Sport. The work was also supported by awards under the Merit Allocation Scheme (project d71) on the NCI National Facility at the Australian National University.

Nomenclature

D Drag force

ρ Density of air

U Fluid velocity

C_D Coefficient of drag

A Frontal area

k Turbulent kinetic energy

ε Turbulent dissipation rate

ω Specific turbulent dissipation rate

y^+ Local mesh non-dimensional wall distance

θ Crank angle

x Streamwise coordinate

y Vertical cross-stream coordinate

z Spanwise cross-stream coordinate

C_DA Drag area

ω_x Streamwise (x) vorticity

References

[1] Grappe, G., Candau, R., Belli, A., and Rouillon, J. D., 1997. "Aerodynamic drag in field cycling with special reference to the Obree's position". *Ergonomics,* **40**, pp. 1299–1311.

[2] Kyle, C. R., and Burke, E., 1984. "Improving the racing bicycle". *Mechanical Engineering,* **105 (9)**, pp. 34–35.

[3] Hanna, R. K., 2002. "Can CFD make a performance difference in sport?". In The Engineering of Sport 4, S. Ujihashi and S. J. Haake, eds., Blackwell Science, pp. 17–30.

[4] Defraeye, T., Blocken, B., Koninckx, E., Hespel, P., and Carmeliet, J., 2010. "Aerodynamic study of different cyclist positions: CFD analysis and full-scale wind-tunnel tests". *Journal of Biomechanics,* **43**, pp. 1262–1268.

[5] Defraeye, T., Blocken, B., Koninckx, E., Hespel, P., and Carmeliet, J., 2010. "Computational fluid dynamics analysis of cyclist aerodynamics: Performance of different turbulence-modelling and boundary-layer modelling approaches". *Journal of Biomechanics,* **43**, pp. 2281–2287.

[6] Defraeye, T., Blocken, B., Koninckx, E., Hespel, P., and Carmeliet, J., 2011. "Computational fluid dynamics analysis of drag and convective heat transfer of individual body segments for different cyclist positions". *Journal of Biomechanics,* **44**, pp. 1695–1701.

[7] Blocken, B., Defraeye, T., Koninckx, E., Carmeliet, J., and Hespel, P., 2013. "CFD simulations of the aerodynamic drag of two drafting cyclists". *Computers and Fluids,* **71**, pp. 435–445.

[8] Menter, F. R., Kuntz, M., and Langtry, R., 2003. "Ten years of industrial experience with the SST turbulence model". In Turbulence, Heat and Mass Transfer 4, K. Hanjalic, Y. Nagano, and M. J. Tummers, eds., Begell House Inc.

[9] Crouch, T. N., Thompson, M., Burton, D., Sheridan, J., and Brown, N. A. T., 2012. "Dominant flow structures in the wake of a cyclist". In Proceedings of the 30th AIAA Applied Aerodynamics Conference, New Orleans, USA.

[10] Crouch, T. N., Sheridan, J., Burton, D., Thompson, M., and Brown, N. A. T., 2012. "A quasi-static investigation of the effect of leg position on cyclist aerodynamic drag". In Proceedings of the 9th Conference of the International Sports Engineering Association, Lowell, USA.

[11] Karabelas, S. J., and Markatos, N. C., 2012. "Aerodynamics of fixed and rotating spoked cycling wheels". *J. Fluids Eng.,* **134**, p. 011102.

[12] Menter, F. R., and Egorov, Y., 2010. "The Scale-Adaptive Simulation method for unsteady turbulent flow predictions. Part 1: Theory and model description". *Flow, Turbulence and Combustion,* **85**, pp. 113–138.

[13] Breuer, M., Jaffrezic, B., and Arora, K., 2008. "Hybrid LES-RANS technique based on a one-equation near-wall model". *Theor. Comput. Fluid Dyn.,* **22**, pp. 157–187.

[14] Bhushan, S., and Walters, D., 2012. "A dynamic hybrid Reynolds-averaged Navier Stokes-Large eddy simulation modeling framework". *Phys. Fluids,* **24**, p. 015103.

[15] Hunt, J., 1987. "Vorticity and vortex dynamics in complex turbulent flows". In CANCAM, Transactions of the Canadian Society of Mechanical Engineers 11, 21.

[16] Sahner, J., Weinkauf, T., and Hege, H.-C., 2005. "Galilean invariant extraction and iconic representation of vortex core lines". In EUROGRAPHICS - IEEE VGTC Symposium on Visualization.

5 Figure Captions

Fig. 1. A picture of the posable experimental mannequin, at a crank angle of $\theta = 0°$.

fig. 2. A sketch of the geometry used in the numerical model, along with the computational domain.

Fig. 3. Plot of C_DA against crank angle for both wind tunnel measurements and ANSYS numerical simulations (points). Also plotted are the angles of each of the thighs from the horizontal, through the crank angle cycle (lines).

Fig. 4. Contours of streamwise vorticity with vectors of cross-stream velocity, for a cyclist at crank angle of 15° (left) and 75° (right), at cross sections $x = -0.04$ m (top), 0.32 m (middle) and 0.60 m (bottom). In each set of three images, results are shown for experimental (left) numerical steady-state (middle) and numerical transient average (right) results. Contours vary across the range $-100s^{-1} \leq \omega_x \leq 100s^{-1}$, from blue (negative) to white (zero) to red (positive).

Fig. 5. At left, contours of streamwise velocity in a plane located at $x = 0.60$ m, for the 15° (top) and 75° (bottom) cases. Middle, the same contours but for an instantaneous field. At right are the corresponding instantaneous streamwise vorticity contours, for the same contour colour levels as in figure 4.

Fig. 6. Contours of time-averaged streamwise velocity taken from the transient SAS-SST numerical simulations, in a plane located at $z = 0$ m, for the 15° (left) and 75° (right) cases. Contours vary across the same scale as shown for the velocity plots in figure 5

Fig. 7. Contribution to total drag area, C_DA, from various sections of the geometry. The vertical dashed line at $\theta = 180°$ represents the halfway point of the crank cycle.

Fig. 8. Left and right perspective views for an instantaneous snap shot of isosurfaces for a single value of the q-criterion, coloured by the cross-stream velocity (blue-negative, red-positive). At top is shown the case for crank angle of 15° and at bottom for 75°.

Fig. 9. Left and right perspective views of isosurfaces for a single value of the q-criterion, coloured by streamwise vorticity (blue-negative, red-positive), but calculated on the velocity field transient average. At top is shown the case for crank angle of 15° and at bottom for 75°.

Fig. 1. figure1.eps

Journal of Fluids Engineering. Received June 19, 2013;
Accepted manuscript posted April 15, 2014. doi:10.1115/1.4027428

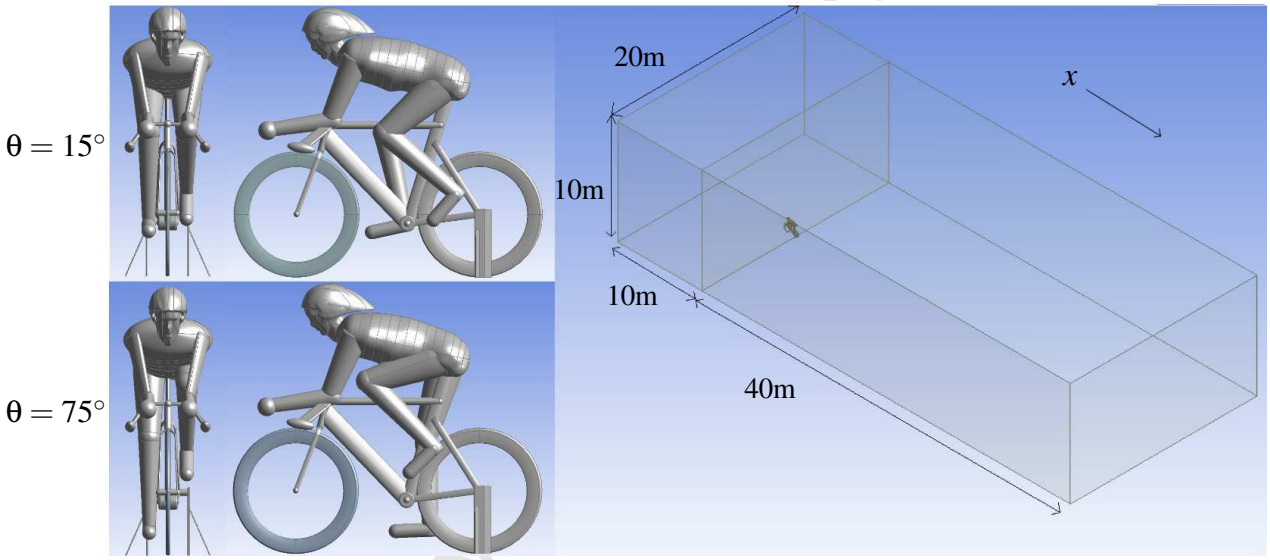

Fig. 2. figure2.eps

Journal of Fluids Engineering. Received June 19, 2013;
Accepted manuscript posted April 15, 2014. doi:10.1115/1.4027428

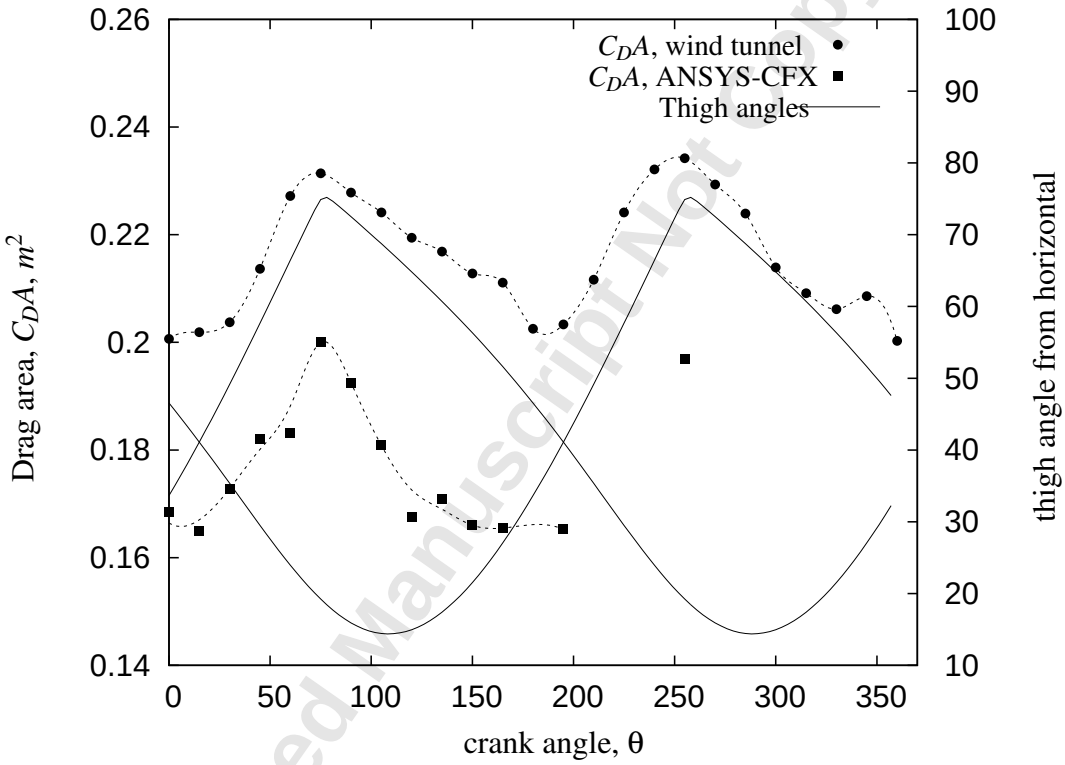

Fig. 3. figure3.eps

Journal of Fluids Engineering. Received June 19, 2013;
Accepted manuscript posted April 15, 2014. doi:10.1115/1.4027428

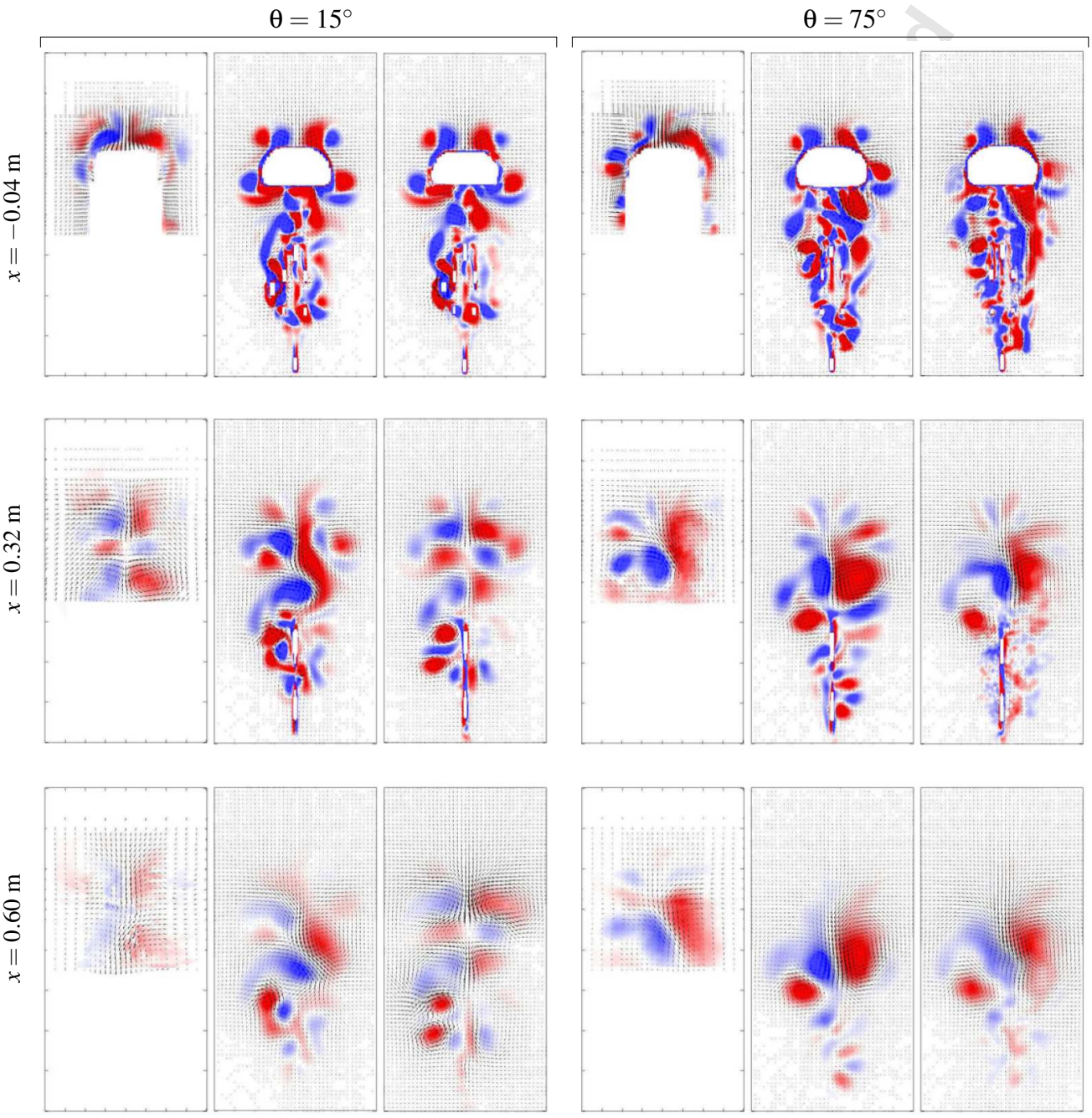

Fig. 4. figure4.eps, figure4_bracket.eps

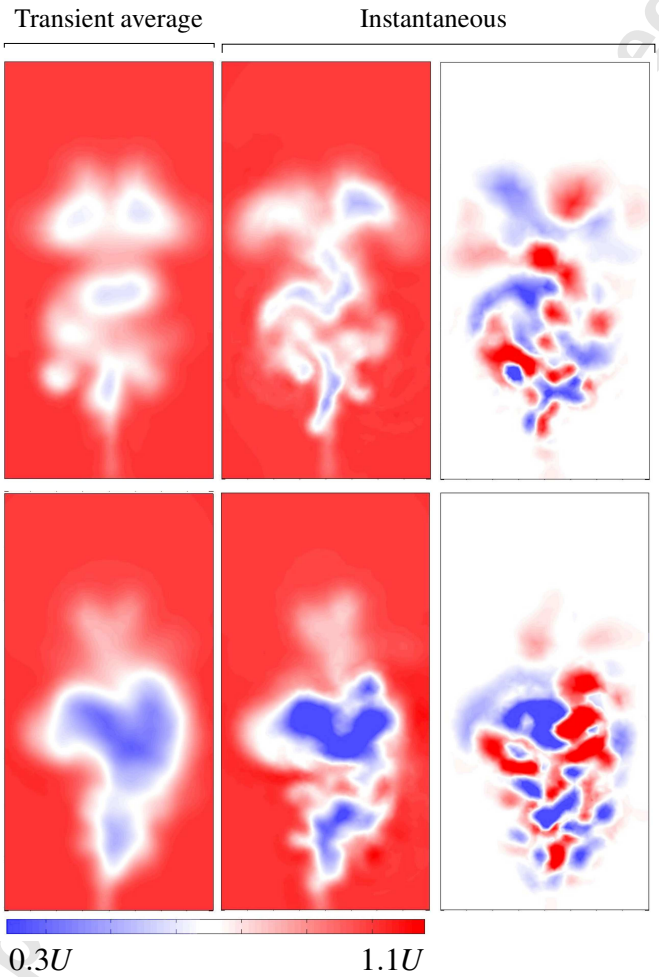

Fig. 5. figure5.eps, figure5_bracket.eps

Journal of Fluids Engineering. Received June 19, 2013;
Accepted manuscript posted April 15, 2014. doi:10.1115/1.4027428

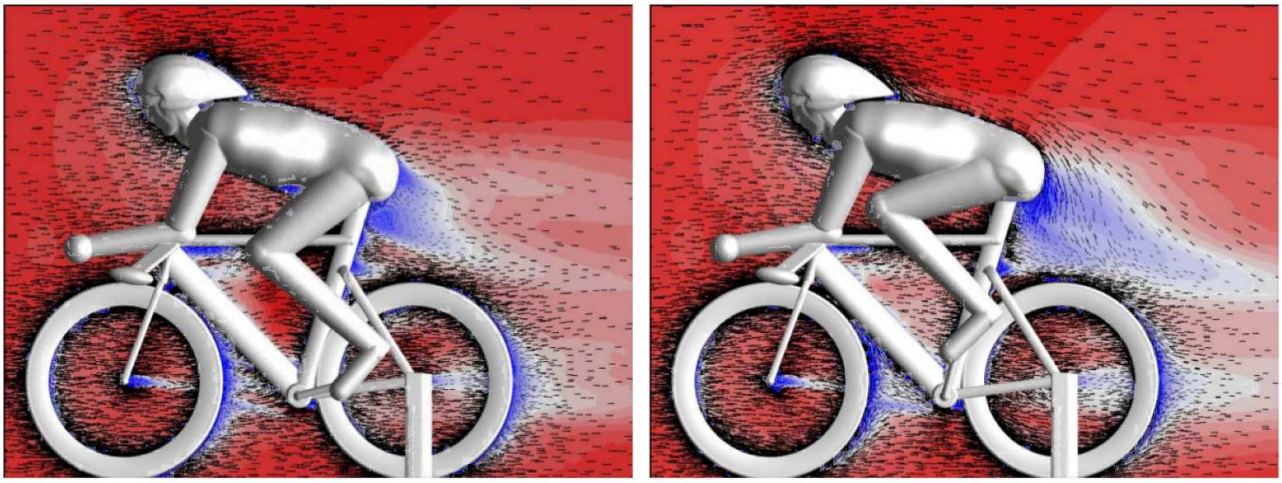

Fig. 6. figure6.eps

Journal of Fluids Engineering. Received June 19, 2013;
Accepted manuscript posted April 15, 2014. doi:10.1115/1.4027428

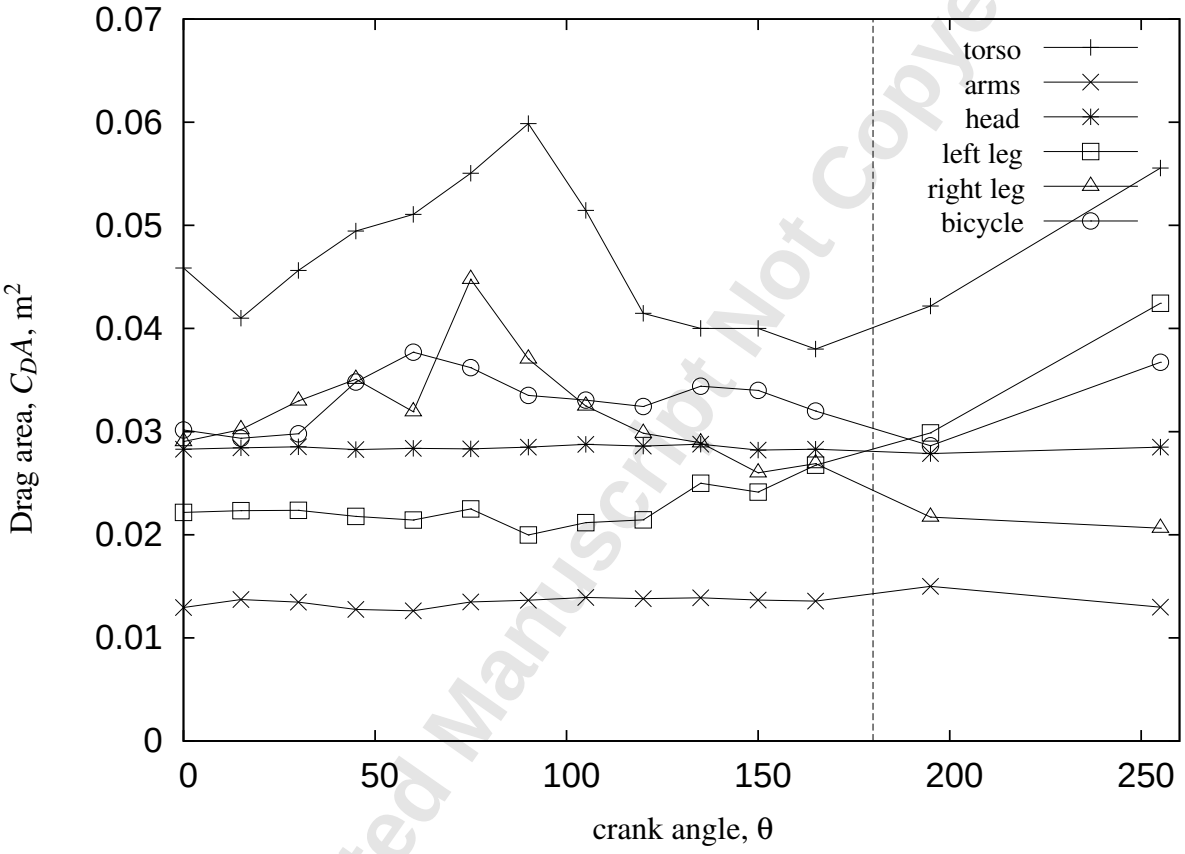

Fig. 7. figure7.eps

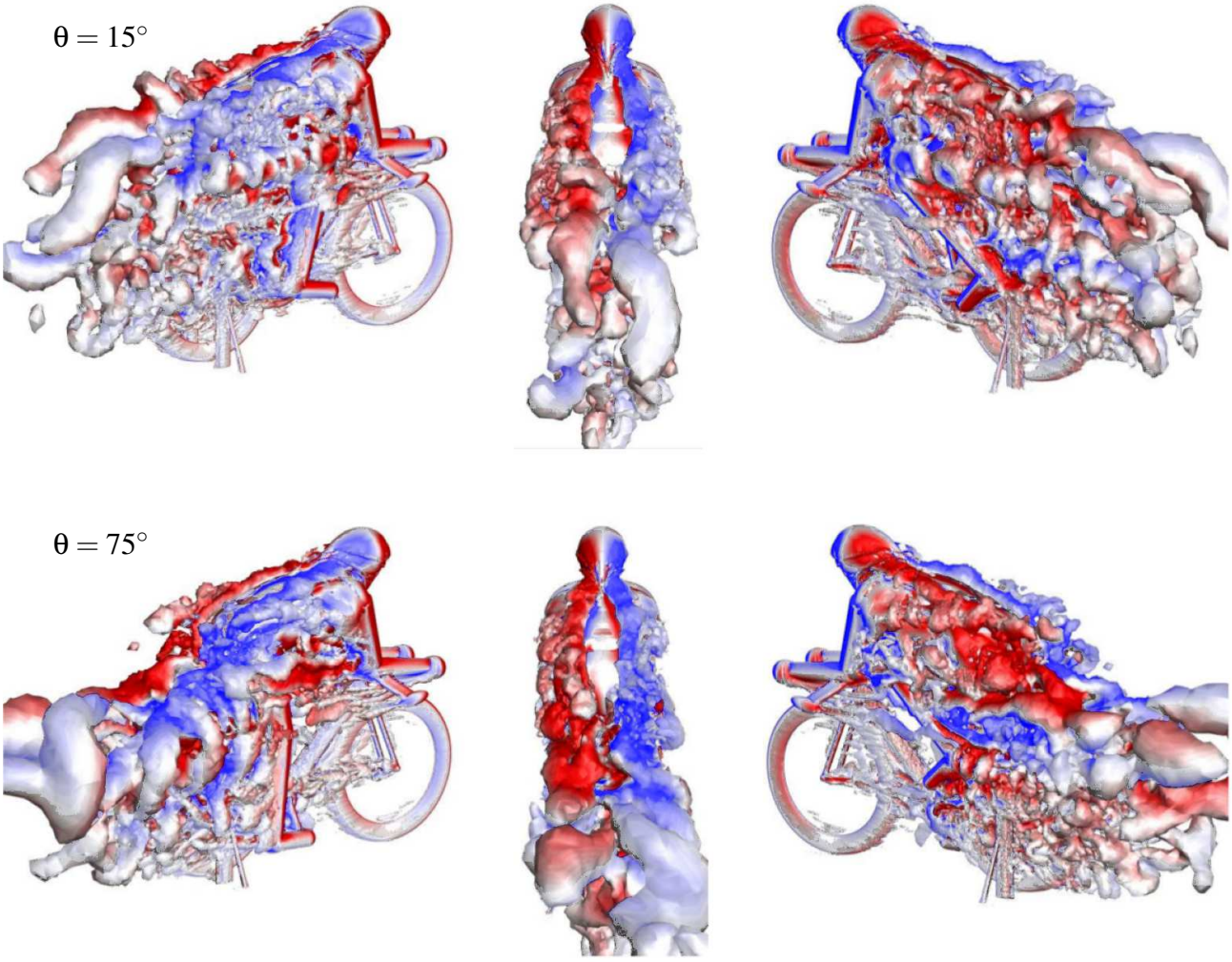

Fig. 8. figure8.eps

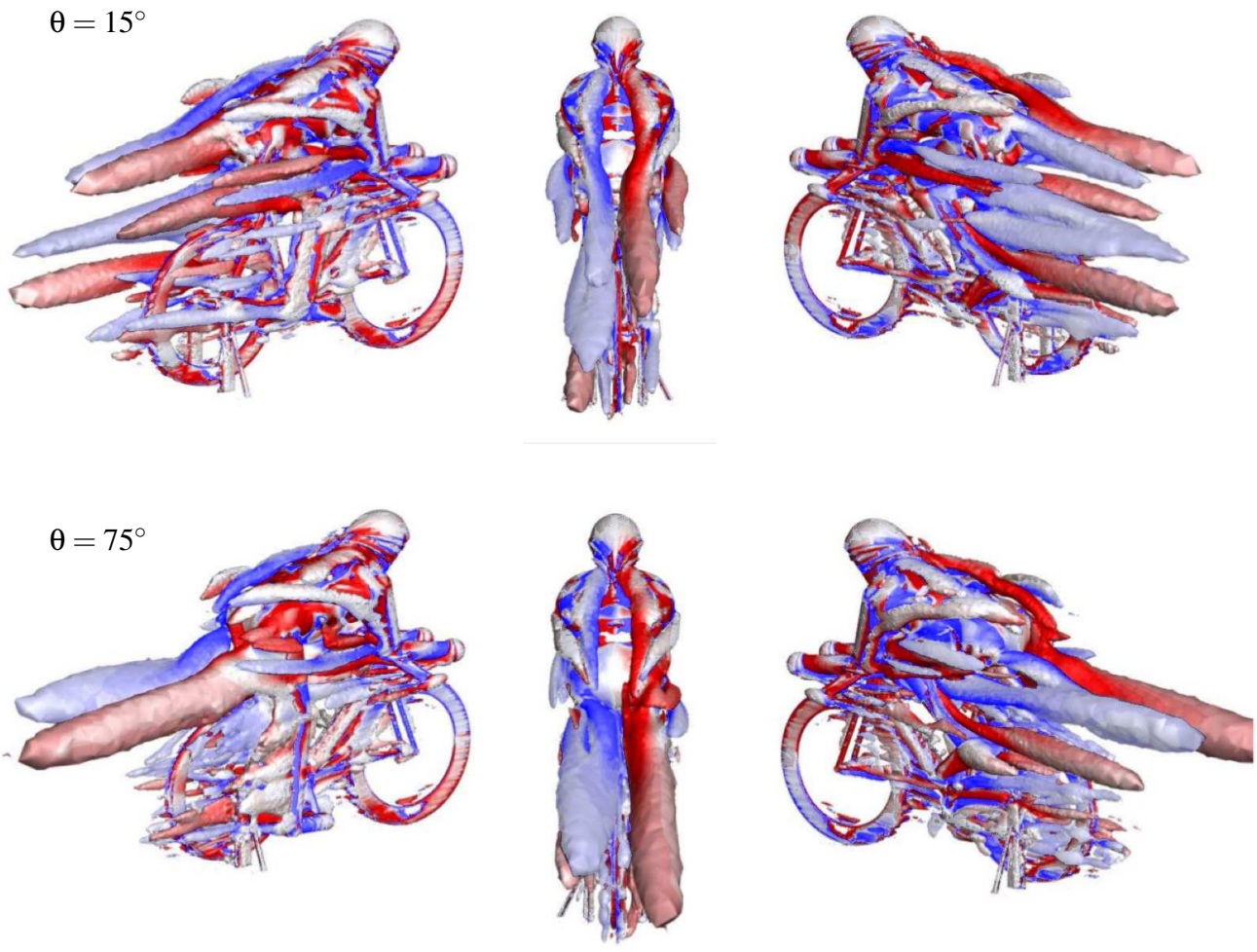

Fig. 9. figure9.eps